The Nature of Native MgO in Mg and Its Alloys

SHIHAO WANG, YUN WANG, QUENTIN RAMASSE, and ZHONGYUN FAN

Native MgO particles in Mg-alloy melts have been recently exploited as potential substrates for heterogeneous nucleation during solidification, leading to significant grain refinement of various Mg-alloys. However, our current knowledge of the nature of the native MgO particles is still limited. In this work, we study both the physical and chemical nature of the native MgO in commercial purity Mg and Mg-9Al alloy by means of advanced electron microscopy. We found that as oxidation products MgO aggregates exist in the alloy melt in three different forms: dominantly young oxide film, occasionally old oxide film and ingot skin, all consisting of discrete nano-sized MgO particles. Detailed analysis shows that the native MgO particles have an octahedral or cubic morphology, a nano-scale particle size and a log-normal size distribution. The mechanisms underlying the formation of the two types of MgO were investigated, and we found that octahedral MgO is formed by oxidation of Mg melt and cubic MgO by oxidation of Mg vapor. With a large lattice misfit with α-Mg, the native MgO particles are impotent for heterogeneous nucleation, but can be made effective for grain refinement.

https://doi.org/10.1007/s11661-020-05740-1

I. INTRODUCTION

To improve fuel economy and reduce CO_2 emissions, it has been reported that Mg-alloys have been regarded as one of the most promising structural materials for automotive applications because of their high specific strength and good castability.[1] However, due to the high affinity of Mg with oxygen, oxidation happens throughout the life cycle of Mg-alloys from the foundry to practical service and recycling.[2,3] Oxidation brings up many problems, such as the presence of oxide impurities in the as-cast products,[4,5] non-protective oxide films for corrosion[6] and a high tendency to ignite and burn when exposed to air at high temperatures.[7] These together with other issues inhibit the widespread application of Mg-alloys.[8–10] Therefore, significant efforts have been directed to understand oxidation mechanisms in Mg-alloys and to develop practical approaches to minimize their negative effects,[11–15] as has been reviewed recently by Czerwinski[16] and Tan *et al.*[17] Extensive practical methods were proposed to either retard or eliminate oxidation. These include the prevention of ignition and burning by applying a flux or protective gas during casting,[18,19] the addition of reactive elements to enhance the oxidation resistance through the formation of protective oxide films,[16, 20] the application of melt cleaning techniques and innovative die filling to ensure the casting quality and mechanical properties of Mg-alloys.[9,21]

Nevertheless, different approaches have also been tried recently to explore potential benefits from the native oxide particles. For example, the oxide particles were found to be exploitable to produce MgO particle-reinforced metal matrix composites,[22] and to serve as substrates for heterogeneous nucleation to refine the as-cast grain structures of Mg alloys.[23–27] Decades ago, MgO was already proposed as a potential nucleating substrate for heterogeneous nucleation of Mg and its alloys.[23] Lee demonstrated that the addition of exogenous MgO particles results in moderate grain refinement in binary Mg-Al alloys.[24] Recently, significant grain refinement of AZ91D alloy[25] and commercial purity Mg (CP Mg)[27] was achieved through manipulating the native MgO particles by means of intensive melt shearing,[28] which was capable of breaking up MgO films into dispersedly distributed particles. The heterogeneous nucleation of α-Mg on MgO particles has been confirmed by the identification of well-defined orientation relationships (ORs) between the faceted MgO particles and α-Mg grains in AZ91D and CP Mg:[25,27,29]

$$\text{OR1}: (111)\left[01\bar{1}\right]\text{MgO} \,//\, (0002)\left[11\bar{2}0\right]\text{Mg}, \quad \text{for } \{111\} \text{ facet};$$

SHIHAO WANG, YUN WANG, and ZHONGYUN FAN are with the BCAST, Brunel University London, Uxbridge, Middlesex, UB8 3PH, UK. QUENTIN RAMASSE is with the SuperSTEM Laboratory, SciTech Daresbury Campus, Daresbury WA4 4AD, UK and also with the School of Chemical and Process Engineering and School of Physics, University of Leeds, Leeds LS2 9JT, UK. Contact e-mail: Zhongyun.Fan@brunel.ac.uk

Manuscript submitted November 28, 2019.
Article published online April 12, 2020

$$\text{OR2}: (100)\left[0\bar{1}1\right]\text{MgO} \;//\; (0\bar{1}12)\left[01\bar{1}1\right]\text{Mg},$$
for {100} facet.

Despite the efforts made to investigate the nature of MgO in Mg-alloys in the literature, our current knowledge about the native MgO films/particles in Mg-alloy melts is limited, and many important questions remain unanswered. Firstly, the physical nature of the oxide films/particles is not adequately characterised. In the Mg-alloy melt, is the oxide film a solid film or a liquid film? Secondly, two kinds of MgO particles different in morphology, namely octahedral MgO (denoted as {111} MgO) and cubic MgO (denoted as {100} MgO), were recently observed in AZ91D and CP-Mg respectively.[25,27,29] Although alloying elements were speculated as the reasons for the morphological transformation from {001} MgO in pure Mg melt to {111} MgO in AZ91D by minimizing the interfacial energy through the adsorption of Al and Zn at the liquid/oxide interface, conclusive experimental evidence is needed. Thirdly, it is of importance to reveal the growth mechanisms of native MgO particles, as their morphology, surface termination, size and size distribution are closely related to the efficiency of both the heterogeneous nucleation and the subsequent grain initiation processes. For grain initiation, the free growth model[30] points out that the size distribution and the number density of inoculants are vital for grain refinement after solidification, and they serve as crucial inputs to determine the as-solidified grain size. Lastly, in terms of heterogeneous nucleation, the atomic arrangement on the terminating surface of MgO particles plays a key role in the nucleation potency since from structural templating point of view the nucleation potency is a function of lattice misfit at the substrate/solid interface,[31] which is usually assessed according to the observed OR between Mg and MgO.[27,29] Therefore, to understand the role of native MgO particles in terms of solidification in Mg-alloys, it becomes necessary to study the nature of native MgO from hierarchical scales, either for the pre-existing oxides and/or newly-generated oxides during the casting process.

In the present work, extensive electron microscopy was carried out to study the native MgO particles in CP-Mg and Mg-9Al alloy in terms of morphology, size and size distribution, as well as the structural and chemical characteristics at the Mg/MgO interface. The mechanism underlying the growth of different types of MgO particles is discussed, along with the effect of the MgO particles on heterogeneous nucleation and grain initiation of α-Mg.

II. MATERIALS AND METHODS

CP-Mg (Mg-0.04Al-0.02Mn-0.013Si, all compositions are in wt pct unless specified otherwise) and commercial purity aluminium (CP-Al, Al-0.04Si-0.06Fe) were used as the raw materials for the alloy preparation in this work.

The amount of alloy melt for each casting was about 1 kg if not specified otherwise. A sliced Mg ingot was first melted in a steel crucible at 700 °C under the protective atmosphere of mixed 99.5 vol pct N_2 and 0.5 vol pct SF_6, followed by holding at the temperature for 2 hours. For Mg-9Al alloy, Al alloying was achieved by adding a certain amount of CP-Al into the Mg melt; stirring was then applied three times before holding at 700 °C. To facilitate direct examination of the oxide films/particles in the melt, a pressurized melt filtration technique[25] was employed to collect the inclusions. The alloy melt, which had been homogenized by the isothermal holding, was transferred to the pre-heated filtration unit isolated from air. Pressure was applied to the melt by introduction of argon gas forcing the liquid metal to flow through a filter attached at the bottom of the crucible. The remaining melt in the crucible solidified steadily afterwards with concentrated oxides left above the filter.

To study the original features of certain types of MgO particles, CP Mg melt in a crucible at 700 °C was exposed to the ambient environment, with simultaneous coverage of protective gas to prevent catastrophic burning. After cleaning away the dross, the protective gas was removed and the melt solidified steadily in the crucible. New oxide films were allowed to form on the fresh melt surface together with a few nodules due to local ignitions. Sampling was therefore made from three positions: (i) the cross-section of the solidified ingot where oxide films were present at the surface; (ii) the crucible wall on which white products were collected and (iii) the nodules on the surface of the solidified ingot where the reaction products were collected. The first sample was prepared by mechanical grinding and polishing as described below. The collected products of the latter two were milled and the powders were then dispersed into ethanol assisted by ultrasonic stirring, resulting in a solution with homogeneously suspended particles, which was then dropped onto a conducting paste and dried in the oven at 150 °C for further characterization.

Samples for metallographic characterization were prepared according to the standard procedure. To minimize any possible artificial interference from the reaction of Mg with water, all used solutions were alcohol-based. Final polishing was performed with a mixture of 0.02 μm colloidal silica suspension and alcohol. The morphology and chemistry of MgO films/particles were characterized by scanning electron microscopy (SEM) using a Carl Zeiss Crossbeam 340 microscope equipped with Inlens Secondary Electron (SE) detector and an energy-dispersive X-ray spectrometer (EDS); the accelerating voltage was 5 kV. The particle size and size distribution were measured directly from multiple SEM images of the MgO particles using image-processing software Fiji Image J.[32]

The specimens for transmission electron microscopy (TEM) and scanning transmission electron microscopy (STEM) analysis were prepared from the slices of the residual material above the filter with concentrated MgO films/particles. The slices were mechanically ground and cut into 3 mm diameter discs, followed by manual polishing down to a thickness about 60 μm; the

final thinning was done by either twin-jet electropolishing or ion beam thinning using a Gatan PIPS system. Conventional bright field (BF) TEM imaging, selected area electron diffraction (SAED), high-resolution transmission electron microscopy (HRTEM) and annular dark-field (ADF) STEM were conducted on a JEOL 2100F instrument operated at an accelerating voltage of 200 kV. Atomic resolution high-angle annular dark-field (HAADF) STEM imaging was carried out in a C_S-corrected Nion UltraSTEM100 instrument operated at 100 kV.

III. RESULTS

A. *Nature of Inclusions in Mg Melts*

Examination (by X-ray diffraction analysis) of the inclusions collected by the filtration from both CP-Mg and Mg-9Al melts revealed that only magnesium oxide exists in the melts, with no other inclusions of significance being found in the samples. Further examination showed that the oxide inclusions have three distinctive types: young oxide films, old oxide films and ingot skins, with their general morphologies being shown in Figure 1.

The young oxide film is believed to originate from the oxidation of the Mg melt on the freshly exposed melt surface for a short period of time. The young oxide film is not a solid film, but effectively a flexible liquid film, which consists of nano-sized oxide particles in a liquid matrix and has an average thickness of 0.5 μm. The incorporation and crumpling of such oxide films in the alloy melt lead to the aggregation of the young oxide films, as shown in Figures 1(a) and (b). Careful examination of the aggregates in the filtered samples revealed that there are no cracks between the young oxide films, suggesting that the oxide films formed on the melt surface are easily wetted by the melt once they are incorporated into the melt, and therefore both sides of the young oxide film are wet. This makes it easy to aggregate oxide films into a rumpled lump of inclusion without gaps inside. This is quite different from the double oxide films observed in Al-alloy melts, which are formed by folding the oxide films with a dry side and a wet side.[9,21]

In contrast, the old oxide film is assumed to be the result of a long-term oxidation of the melt surface despite the protective atmosphere. As shown in Figures 1(c) and (d), the old oxide films consist of coarse particles (about 1 μm in average size) on one side that contains elements of the protective gas, such N and F. The coarse oxide particles form a relatively dense scull on the local melt surface, and further oxidation of the melt underneath the scull takes place through the supply of oxygen *via* the cracks in the scull, forming finer oxide particles beneath the old oxide film. Compared with the young oxide films, the old oxide films are relatively stiff, and do not easily form aggregates.

The third type of oxide aggregates found in this work is the ingot skin, which appears in the alloy melt as straight segments (Figures 1(e) and (f)). As inferred by its name, the ingot skin originates from the oxidation at the surface of the Mg ingot in the solid state and brought into the alloy melt. Ingot skins in the melt consist of densely populated nano-scale oxide particles in a liquid matrix, being similar to young oxide films. However, in contrast to the young oxide films, ingot skins are relatively stiff and can keep their straight shape in the melt.[25]

It should be pointed out that the three types of oxide aggregates are inherent to Mg-alloys and independent of the alloying elements. However, the relative proportions of the three aggregates are quite different. Young oxide films were dominant in quantity among the three types of oxide aggregates, while old oxide films and ingot skins were rarely observed. For this reason, we focus our investigation here onwards mainly on the young oxide films.

B. *Nature of MgO Particles*

As shown by SEM in Figure 2, the size of the oxide particles in young oxide films ranges from 50 to 100 nm in diameter. Further examination indicated that there exist two types of particles differing in morphology: polyhedral (Figures 2(a) and (c)) and cubic shapes (Figures 2(b) and (d)), both of which were observed in CP-Mg and Mg-9Al alloy. The EDS analyses in Figures 2(e) and (f) show that the particles primarily contain magnesium and oxygen, indicating that these are MgO particles. The deviation of EDS-measured Mg/O atomic ratio from unity is attributed to the inclusion of Mg matrix in the e-beam/specimen interaction volume during the EDS acquisition. The presence of carbon peaks in the EDS spectra is the result of adventitious carbon contamination during SEM examination rather than being intrinsic to the particles.[33]

More features about the young MgO film were provided by TEM examinations. The bright field (BF) TEM images in Figures 3(a) and (c) show the particle arrangements in oxide films collected from CP-Mg and Mg-9Al, respectively. The corresponding selected area electron diffraction (SAED) patterns (from areas comprising numerous particles) are presented in Figures 3(b) and (d), where the ring patterns suggest that the oxide particles are randomly orientated inside the Mg matrix. Indexing the ring patterns (Table I) confirms that the oxide particles are MgO that has a FCC crystal structure ($Fm\bar{3}m$ space group) with a lattice parameter of $a = 4.211$ Å.[34] The additional diffraction spots in Figure 3(d) are from an β-$Mg_{17}Al_{12}$ intermetallic phase being viewed along its [001] direction.

Deep etching to remove the Mg matrix by electropolishing was carried out to reveal the three-dimensional (3D) morphology of the MgO particles. As shown in Figure 4(a), a MgO particle with five facets is clearly displayed, with additional facets at the back obstructed from the view due to the projection. Based on this morphology, specific symmetries are observed: the configuration of the four side facets (*i* to *iv*) shows a

4-fold symmetry around the normal of the small 'top' facet (*v*), while each side facet (*i* to *iv*) itself shows a 3-fold symmetry around its own normal.

The exact crystallography of the facets on these MgO particles was further determined by TEM characterization. The BF image in Figure 4(b) shows two MgO particles having sharp interfaces with α-Mg, which are precisely illustrated by the corresponding HRTEM images from [011] and [112] MgO zone axes in Figures 4(c) and (d), respectively. The first two rows in Table II give the measurements of *d*-spacings and interplanar angles, which are in good agreement with the corresponding values calculated from the reported crystal structure of MgO in the literature.[34] The indexed HRTEM images provide crystallographic information about the truncated surfaces of the two MgO particles. The particle on the left-hand side in Figure 4(b) is faceted with four $\{111\}_{MgO}$ planes and two $\{100\}_{MgO}$ planes in projection along the $[110]_{MgO}$ direction. In contrast, the other particle has two {111} facets left since the particle is viewed along a $[112]_{MgO}$ direction, 30 deg away from the former axis rotating around the $\langle 111\rangle_{MgO}$ axis. The identified {111} and {100} facets of MgO have 3- and 4-fold symmetry, respectively, which is consistent with the symmetry observed in Figure 4(a).

Combining the information on morphology and crystallography of the truncated facets of the particles, it can be concluded that such MgO particles exhibit possible morphologies ranging from a cuboctahedron (eight {111} facets plus six {001} facets) to an octahedron (eight {111} facets) depending on how many {100} facets remain when the growth stops. According to the Wulff construction,[35] for a MgO crystal consisting of {111} and {100} facets only, the transition from cuboctahedron to octahedron then can be achieved by altering the relative length of the surface normal of each facet, which is proportional to the surface energy. As demonstrated in Figures 5(a), the three MgO particles labelled as 1, 2 and 3 can be well matched by the reconstructed schematics in Figures 5(b), (c) and (d), respectively. It is seen that the {001} facets become narrower with increasing particle size. For simplicity, this kind of MgO is hereafter named as octahedral MgO and denoted as {111} MgO.

The 3D morphology of the cubic MgO particles was also revealed by deep etching through electropolishing. As shown by SEM imaging in Figure 6(a), a large cubic particle is seen being attached to several smaller cubes. TEM observations in Figure 6(b) shows two cubic particles with the inset being the SAED pattern indexed as MgO along its [001] zone axis. The corresponding HRTEM image (Figure 6(c)) and its indexing (the third row in Table II) confirm the identification of the phase as MgO with {100} terminating facets. According to these observations and the 4-fold symmetry of the particle, it is concluded that the cubic MgO is truncated by six {100} facets. This kind of MgO is henceforth termed as cubic MgO and denoted as {100} MgO.

C. *The Chemical and Structural Configuration at the Surface of MgO*

Figures 7(a) through (d) show an ADF STEM image and the corresponding EDS elemental maps acquired across the MgO/Mg interface in Mg-9Al. The evenly distributed Al signal in Figure 7(d) suggests no Al preferential segregation at the interface. Figure 7(e) shows the BF TEM and SAED pattern of a {111} MgO particle in CP Mg, whose surface is atomically flat as revealed by the atomic-resolution HAADF STEM image in Figure 7(f). In addition, the relatively uniform contrast across the interface excludes the adsorption or segregation of trace impurities such as Mn and Si (whose atomic number would be higher than that of Mg, $Z > 12$ (Mg), and which would therefore appear brighter in this type of chemically sensitive images) at the interface. Similarly, a {111} MgO particle from Mg-9Al was examined as shown in Figures 7(g) and (h). The contrast profile across the MgO/Mg interface in the HAADF image in Figure 7(h) is comparable to that in CP Mg (Figure 7(f)). Also, the lattice structure of MgO is seen to be unchanged at the surface area when Al is present in the melt.

D. *Particle Size and Size Distribution*

To quantify the size and size distribution of the MgO particles, about 1500 particles, either {111} or {100} faceted particles, were measured for the CP-Mg and Mg-9Al alloy. The results given in Figure 8 show that the size distributions follow a log-normal function, with a small difference in the geometric mean diameter d_0 and standard deviation σ. The mean size d_0 of the {100} MgO particles was measured to be 85 nm and 94 nm in CP Mg and Mg-9Al, respectively, both slightly larger than that of the {111} MgO particles being 68 nm in CP Mg and 84 nm in Mg-9Al. With the addition of 9 pct Al, the average size d_0 for both {100} MgO and {111} MgO increased slightly, and the standard deviation σ decreased marginally. This suggests that the addition of Al has little effect on the size and size distribution of MgO particles in the Mg melt.

E. *MgO Detected in Different Positions*

To study the origin of {111} MgO and {100} MgO, CP Mg melt was steadily solidified in crucible to maintain the features of oxidation. Figure 9 shows the comparison between products from the crucible wall (Figure 9(a)) and the surface nodules (Figure 9(b)), where both products exhibit the same cubic morphology. No {111} MgO was observed in such positions in this work.

Figure 10(a) shows the microstructure on the cross section of the CP Mg ingot, on whose surface a compact oxide film is identified. Such an oxide film containing some amounts of F on the surface (as evidenced from the EDS analysis, Figure 10(b)) prevents further oxidation of the melt. By contrast, some areas on the melt surface were found experiencing more oxidation without nodule features. As shown in Figure 10(c), cracks

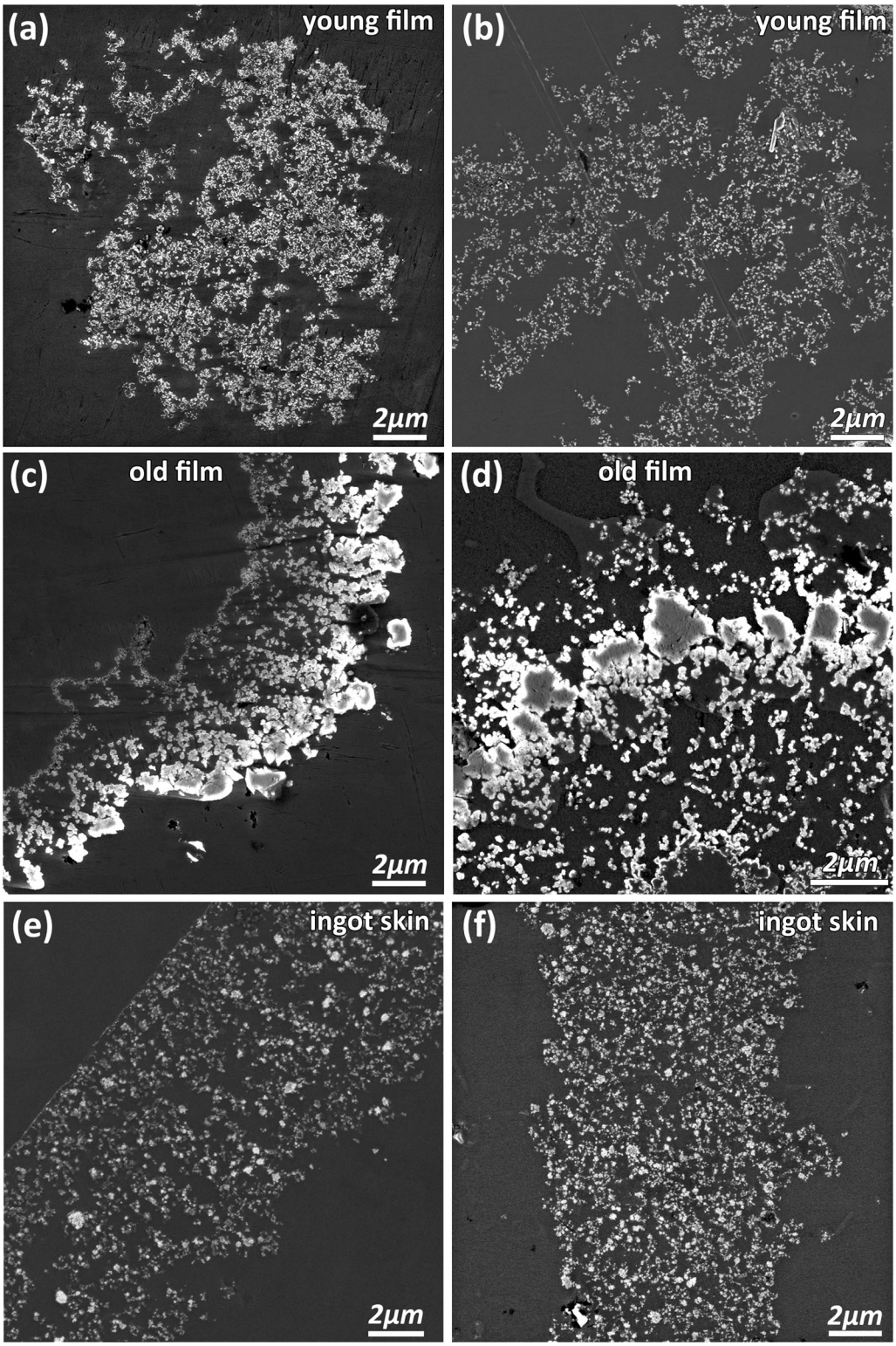

Fig. 1—SE SEM images showing the morphology of MgO films/particles collected by melt filtration from (*a*, *c*, *e*) CP-Mg and (*b*, *d*, *f*) Mg-9Al alloy. (a, b) young films; (c, d) old films; and (e, f) ingot skins.

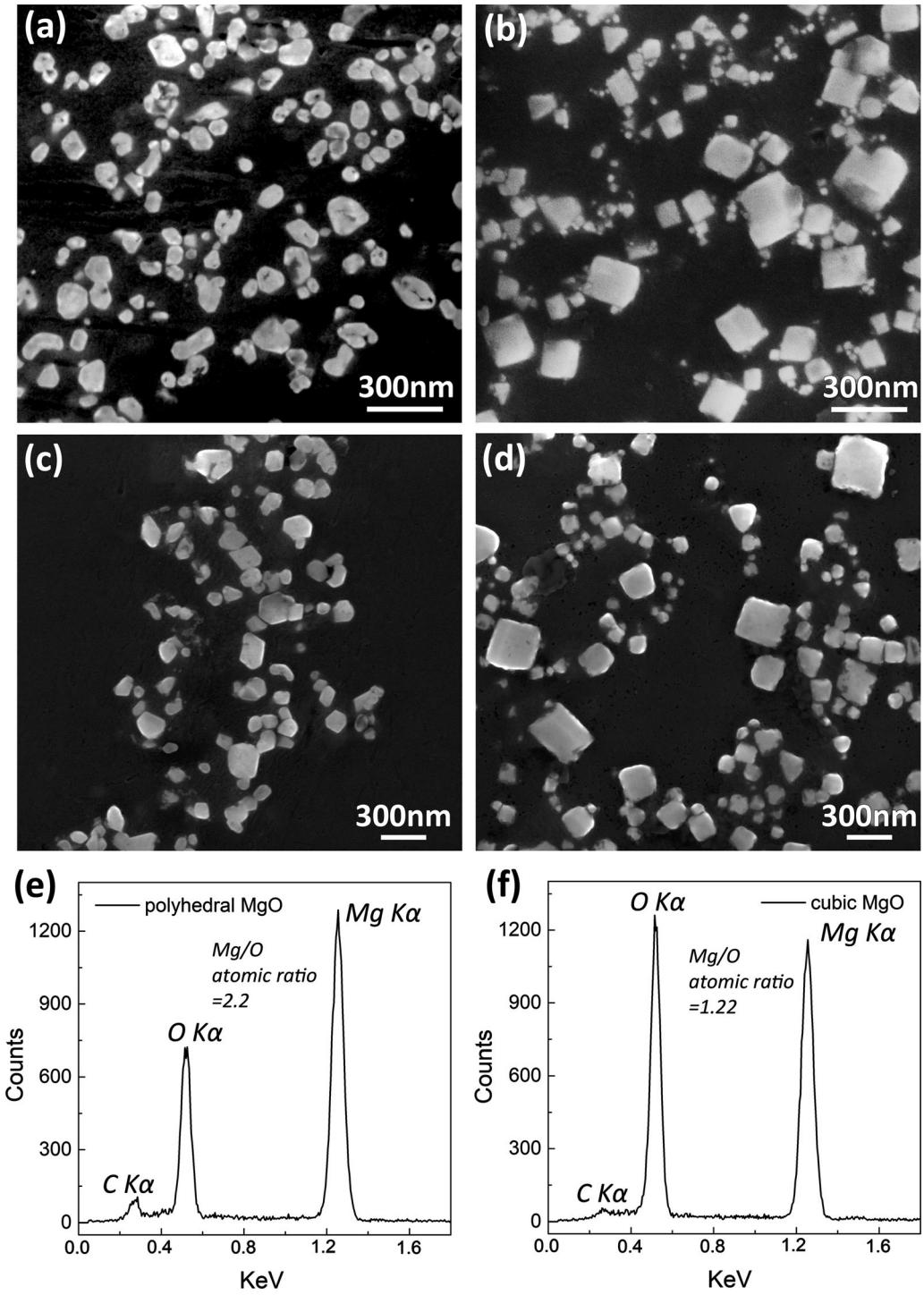

Fig. 2—SE SEM images showing the morphology of (*a*, *c*) polyhedral shaped and (*b*, *d*) cubic MgO particles collected from (a, b) CP Mg or (c, d) Mg-9Al alloy; and (*e*, *f*) EDS spectra acquired from the polyhedral and cubic particle, respectively.

appear on the MgO film with 100 to 200 nm in thickness, which provides routes for the transport of oxygen to the melt-oxide interface; and Mg vapor to the oxide/air interface. Oxidation was thus promoted, resulting in either a thickening of the oxide film or the formation of embedded MgO particles. The polyhedral profile of the particles observed in Figure 10(c) is believed to be the projection of their octahedral shape based on the results in Sections III–A and III–B. Furthermore, it is important to note that no shape of feature would be characteristic of cubic MgO observed in Figure 10(c).

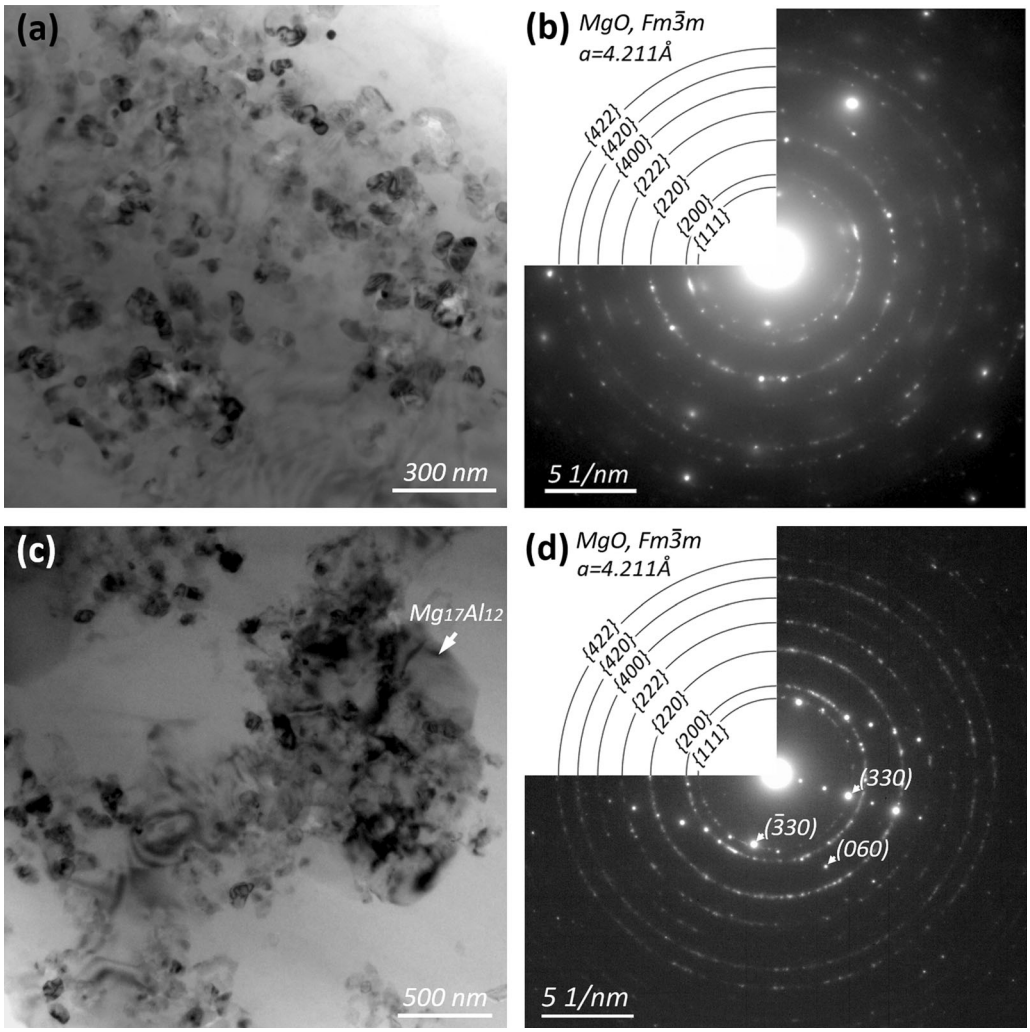

Fig. 3—TEM characterization of the MgO films being composed of densely populated particles in specimens of (*a*, *b*) CP-Mg and (*c*, *d*) Mg-9Al alloy. (a, c) BF TEM images; and (b, d) SAED patterns taken from the MgO films shown in (a) and (c), respectively. Note that the large phase marked in (c) is identified as an β-$Mg_{17}Al_{12}$ phase reflected in (d) with diffraction spots belonging to its [001] SAED pattern.

IV. DISCUSSION

A. *Oxide Films/Particles in Mg-Alloys*

Oxidation has been a major barrier preventing wider-range applications of Mg-alloys. To overcome this drawback, efforts have been directed to the study of the oxidation mechanism at elevated temperatures and under different atmospheres, with many methods being proposed to enhance oxidation resistance. With a view to utilizing native oxides specifically, however, this study focuses on the investigation of their nature in hierarchical scales, *i.e.*, from the micron scale to the nano-scale. At the micron scale, they can be classified as young film, old film and ingot skin according to their morphology (Figure 1), all of which are composed of discrete MgO particles (Figures 1 through 3). The formation mechanism of the young film is proposed as shown schematically in Figure 11. Oxidation happens quickly on the fresh melt surface when it is exposed to air (Figures 11(a) and (b)), forming a thin liquidus oxide film containing discrete MgO particles. The film is easily folded and entrapped into the melt by external or internal vibrations, which exposes some fresh melt to the air again (Figure 11(c)). The ongoing process of folding and tangling results in the agglomeration of the oxide films with micron scales (Figure 11(d)). New oxide film forms on the fresh melt surface and the circulation starts over again. Young film and old film are of course correlated, when a young film is allowed to grow for a long period of time, it eventually becomes an old film, appearing as a curved feature since folding becomes difficult (Figures 1(c) and (d)).

The ingot skin exhibits very different features as a straight segment (Figures 1(e) and (f)),[25] indicating that this type of film is more difficult to be folded during casting. In other words, it is thick enough to prevent it from being crumpled. This type of oxide film was rarely detected in the melts studied in this work. It is believed that the ingot skin comes from solid-state oxidation at the surface of the original ingot, during ambient temperature storage or heating in the furnace before melting.

Table I. Comparison Between the Values of Measured and Calculated *d*-Spacings of MgO

Measured *d*-Spacings in Fig. 3(b) (Å)	Measured *d*-Spacings in Fig. 3(d) (Å)	Calculated *d*-Spacings (Å)*	Crystal Plane {*hkl*}
2.443 ± 0.004	2.460 ± 0.019	2.431	{111}
2.110 ± 0.011	2.117 ± 0.008	2.106	{200}
1.497 ± 0.007	1.501 ± 0.012	1.489	{220}
1.223 ± 0.008	1.228 ± 0.009	1.216	{222}
1.058 ± 0.008	1.021 ± 0.044	1.053	{400}
0.947 ± 0.007	0.924 ± 0.035	0.942	{420}
0.865 ± 0.006	0.863 ± 0.005	0.860	{422}

*Calculated according to the lattice parameter of MgO $a = 4.211$ Å reported in the literature.[34] The *d*-spacings were measured from the SAED ring patterns in Figs. 3(b) and (d) along three directions (0, 45 and 90 deg from horizontal), yielding the average values and standard deviations.

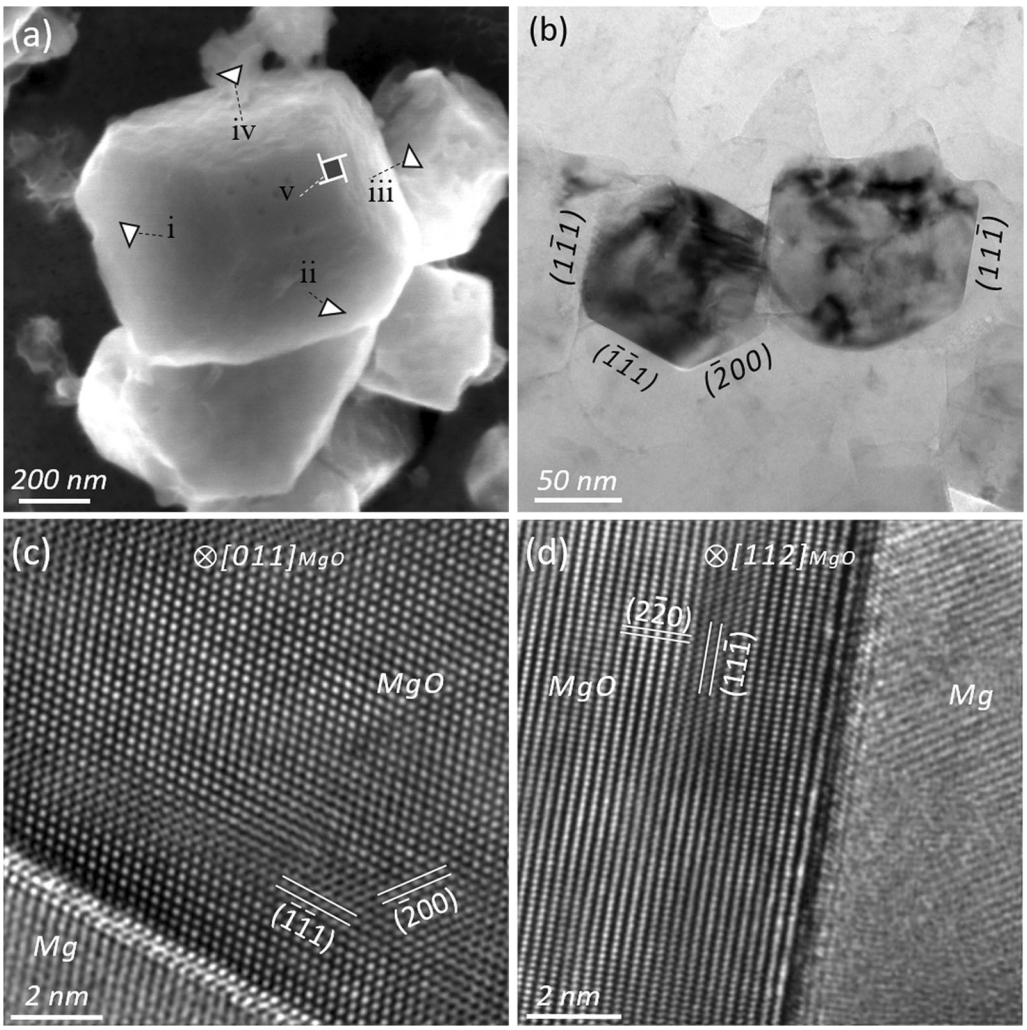

Fig. 4—Identification of octahedral MgO in Mg-9Al by SEM and TEM examinations. (*a*) SE SEM image displaying the faceting morphology of polygonal MgO particles; (*b*) BF TEM image showing the projection of two MgO particles; and (*c*, *d*) the corresponding HRTEM images of the two MgO particles in (b) with zone axis of $[011]_{MgO}$ and $[112]_{MgO}$ direction, respectively.

B. *Formation Mechanism of {100} MgO*

MgO films in Mg and its alloys have been extensively studied,[4,12,36–38] but little of the prior work focused on MgO particles themselves. Recent studies by Fan *et al.*[25] and Wang *et al.*[27,29] confirmed that the native MgO films in melts of Mg and its alloys consist of numerous discrete MgO particles, being either {100} faceted or {111} faceted. The mechanism of the morphological transition from cube to octahedron was proposed as the decrease of interfacial energy probably through adsorption or segregation of Al or/and Zn on the faceted planes.[27] However, both octahedral and cubic MgO particles have been found in CP-Mg and in Mg-9Al alloy in this work (Figure 2), with a similar size

Table II. Comparison Between the Values of Measured and Calculated *d*-Spacings of MgO, As Well As the Angles Between Specific Crystal Planes

Zone [*uvw*]	Axis	Crystal Plane {*hkl*}	Measured *d*-Spacing (Å)	Calculated *d*-Spacing (Å)*	Measured Angle (°) Between Crystal Planes	Remarks
[011]		{111}	2.430 ± 0.014	2.431	70.5, $\langle(\bar{1}\bar{1}1), (1\bar{1}1)\rangle$	Fig. 4(c)
		{200}	2.082 ± 0.018	2.106	54.7, $\langle(\bar{2}00), (\bar{1}\bar{1}1)\rangle$	
[112]		{220}	1.502 ± 0.014	1.489	90, $\langle(11\bar{1}), (2\bar{2}0)\rangle$	Fig. 4(d)
[001]		{020}	2.111 ± 0.022	2.106	90, $\langle(200), (020)\rangle$	Fig. 6(c)

*Calculated according to the lattice parameter of MgO a = 4.211 Å reported in the Ref. [34].

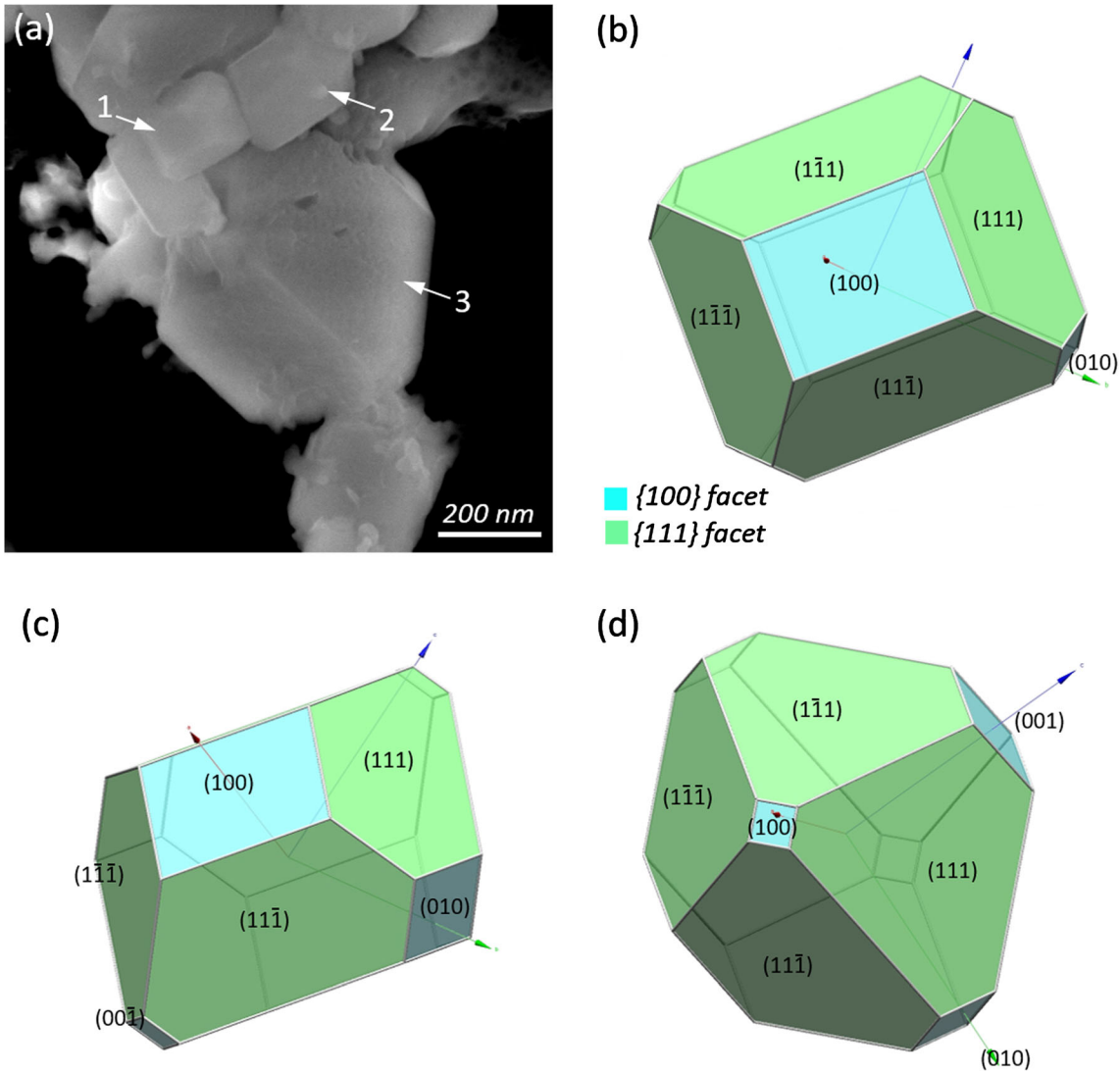

Fig. 5—(*a*) SE SEM image showing a few of octahedral MgO particles; (*b* through *d*) the related schematics showing good matches with the corresponding particles 1, 2 and 3 in (a), respectively. The schematics were built using KrystalShaper software (©JCrystalSoft), with alteration the ratio of the surface normals ($|\mathbf{n}_{\{111\}}|/|\mathbf{n}_{\{100\}}|$) for a crystal faceted by {111} and {100} only.

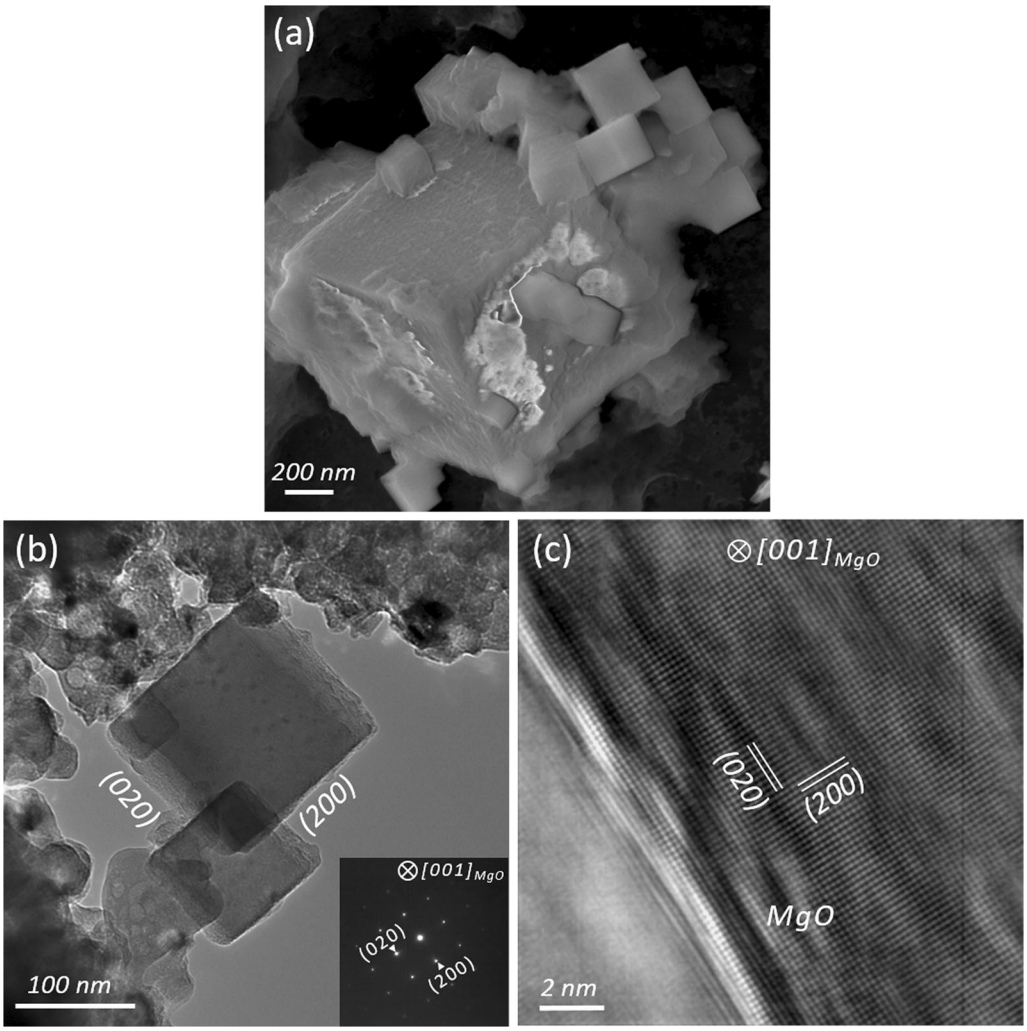

Fig. 6—(*a*) SE SEM image displaying the morphology of a large cubic MgO particle attached by small ones; (*b*) BF TEM image showing two cubic MgO particles with the related SAED pattern (inset); and (*c*) the corresponding HRTEM image acquired at the edge with electron beam parallel to $[001]_{MgO}$ direction.

distribution (Figure 8). This implies that the addition of Al should have little effect on the faceting behavior of the MgO particles, and that the formation of the two types of MgO particles might result from the nature of oxidation of the Mg melt.

Extensive experimental evidence supports the thermodynamic stability of cubic MgO particles with only {100} terminations.[39–41] In the 1940s, MgO crystals prepared by burning a Mg strip in a dry environment were found to be of cubic shape by electron microscopy.[39] This was consistent with the theoretical calculation of the Madelung potential and density functional theory (DFT) results, whereby the surface state for the {100} plane of MgO was found to be the most stable amongst all lattice planes.[40,41] Given the calculated surface energies, Wulff's reconstruction theory[35] indicates a thermodynamic equilibrium shape of MgO terminated by its {100} planes. However, the shape of a crystal is determined not only by the equilibrium thermodynamics but also by the kinetics of the system. The self-sustaining severe oxidation of Mg in the vapor phase seems to be a thermodynamics-controlled process, as the high temperature and the reservoir of Mg and O vapors ensure that the rate of atomic/molecule attachment will not be a limiting factor at all. Such a mechanism seems to be followed by the formation of cubic MgO in this study as well. During the casting of Mg and Mg-9Al alloy in this work, similarities to the production of cubic MgO through combustion, such as very local burning, were occasionally observed due to the specific features of Mg above the liquidus: (i) a high affinity with oxygen, (ii) a high vapor pressure and (iii) the absence of protective oxide film. The fact that MgO particles collected from crucible wall and nodules are all cubes (Figure 9) with similar size to those inside the melt (Figures 2(b) and 8) indicates the same origin for all these {100} MgO particles. Their formation follows the mechanism of forming thermodynamically stable MgO in a cubic shape by vapor reaction under ignition conditions. It is

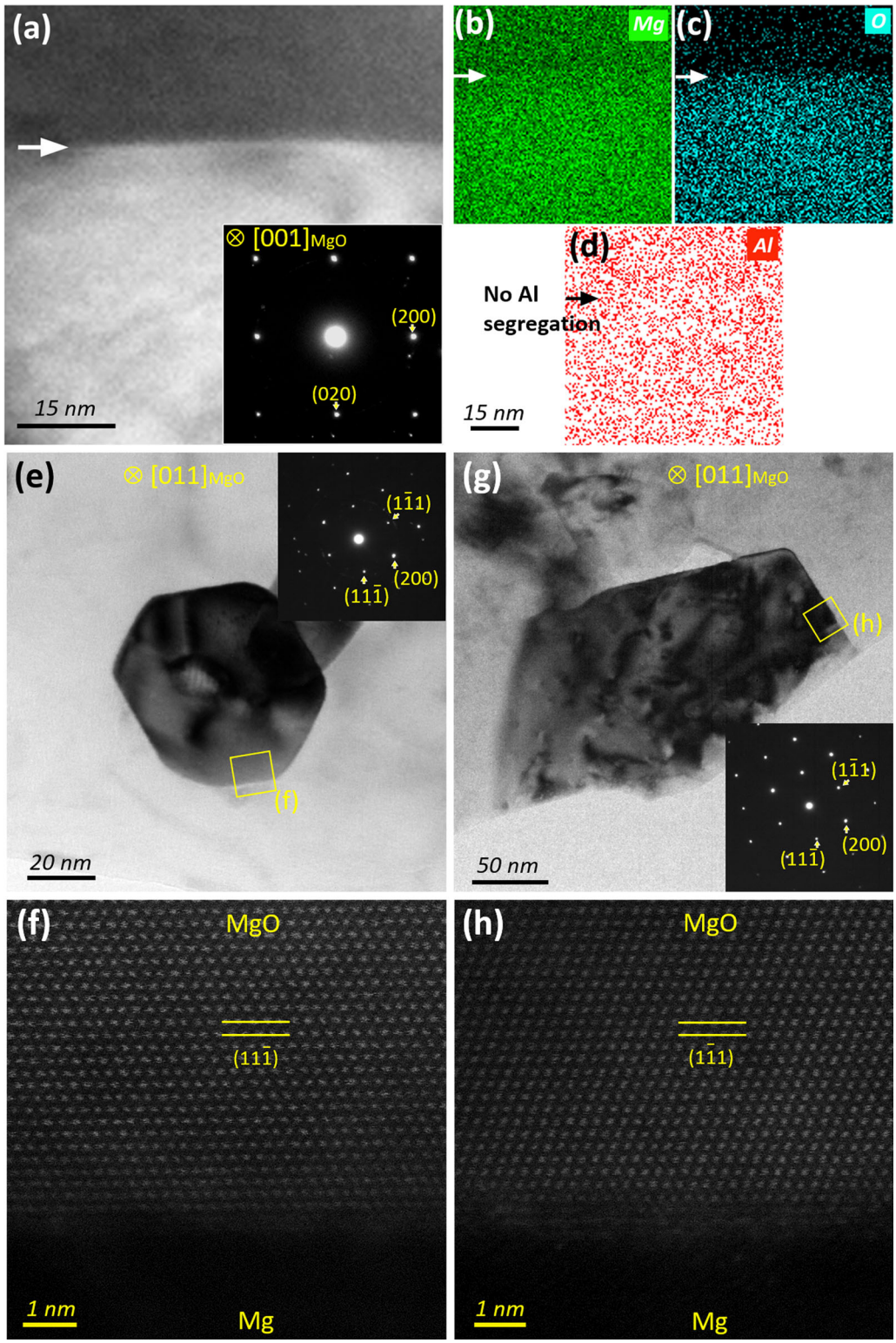

Fig. 7—(*a*) ADF STEM image and EDS elemental maps of (*b*) Mg, (*c*) O and (*d*) Al across the MgO/Mg interface in Mg-9Al alloy; and (*e* through *h*) BF TEM and HAADF STEM images of the {111} MgO in (e, f) CP Mg and (g, h) Mg-9Al, respectively. The insets in (a), (e) and (g) are the corresponding SAED patterns.

worth mentioning that no {111} MgO was ever observed in the particles collected from the crucible wall and nodules in this work, which suggests that the formation mechanism of {111} MgO is different.

The formation mechanism for {100} MgO is also valid for those cubic particles found in Mg-9Al alloy, where ignition and burning in local areas are believed to be inevitable during melt handling and casting.

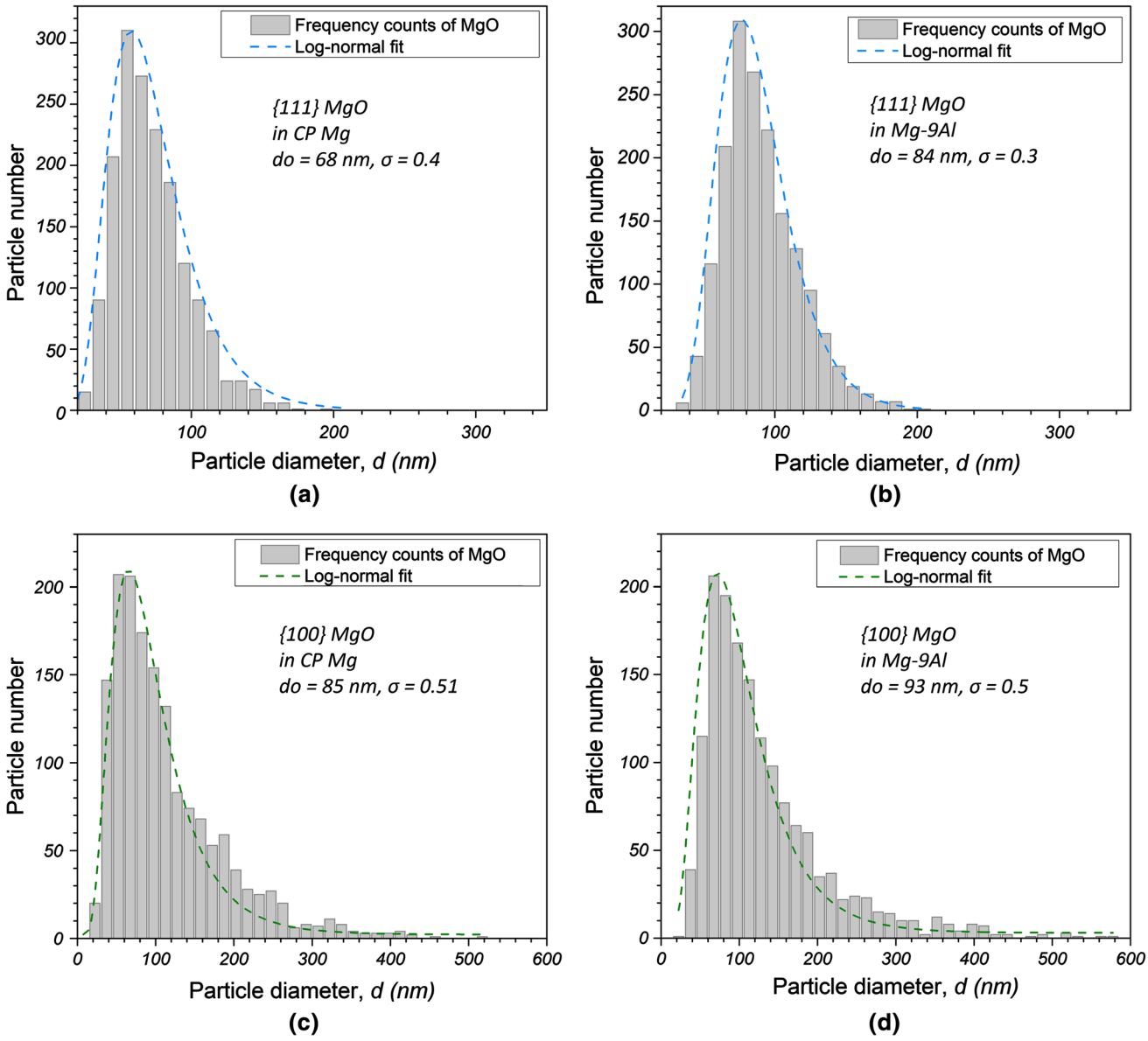

Fig. 8—Statistics of the size distribution for (*a*, *b*) {111} and (*c*, *d*) {100} MgO particles in (a, c) CP-Mg and (b, d) Mg-9Al alloy.

However, due to the enhanced resistance of Mg to evaporation after Al addition, the tendency to burning decreases greatly. As a result, the relative fraction of {100} MgO particles in the Mg-9Al alloy is lower than that in CP-Mg. It is therefore not surprising that the presence of {100} MgO particles has not been reported previously in AZ91D alloy,[25] while no {111} MgO particles were reported in CP Mg either,[27,29] due to their scarcity.

C. *Formation Mechanism of Octahedral {111} MgO*

Octahedral {111} MgO particles have been observed previously in AZ91D alloy,[25,29] where the formation mechanism was proposed as relying on the possible adsorption of Al and/or Zn onto {111} surfaces. The surface energy of a crystal can be modified in terms of thermodynamics,[42] for instance by surface facet tailoring through a surface-regulating agent, as reviewed in detail recently by Zhang *et al.*[43] However, the possibility of elemental adsorption or segregation of solutes at the surface appears to be ruled out by the EDS chemical maps (Figures 7(b) through (d)) and the HAADF analysis (Figure 7(h)); neither Al segregation nor structural change appears at the MgO surface. As a result, the formation of {111} MgO is believed to be independent of the presence of Al, which can be also corroborated by the appearance of octahedral {111} MgO in CP-Mg (Figures 2(a) and 3(a)).

The formation mechanism for {111} MgO should be different from that for {100} MgO, as {111} MgO was not detected at either the crucible wall or the nodule positions (Figure 9). The possible difference in terms of the oxidation process is that the {111} MgO forms at the melt surface without the involvement of any ignition and Mg vapor. Without burning features on the surface

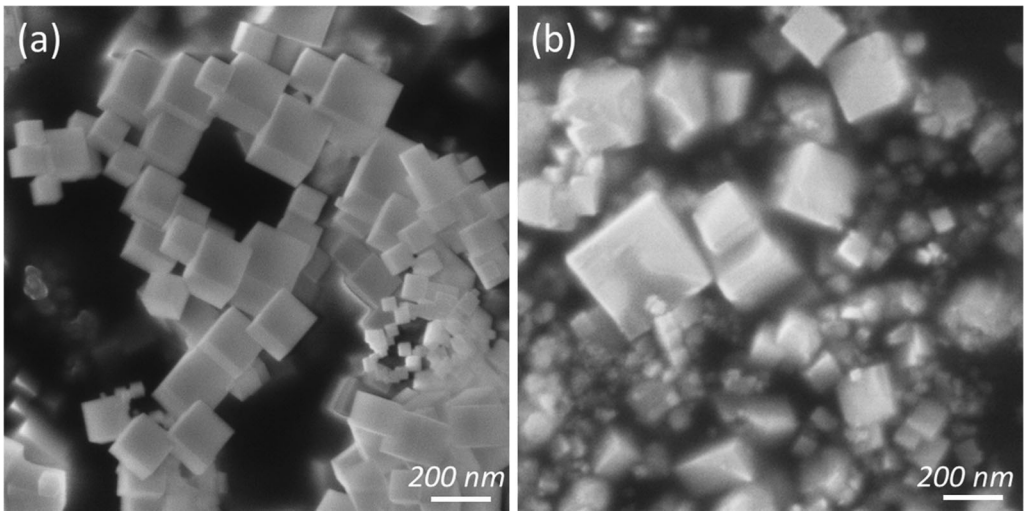

Fig. 9—SE SEM images showing the cubic MgO particles collected from (*a*) the crucible wall and (*b*) the nodule positions on the surface of solidified CP-Mg ingot.

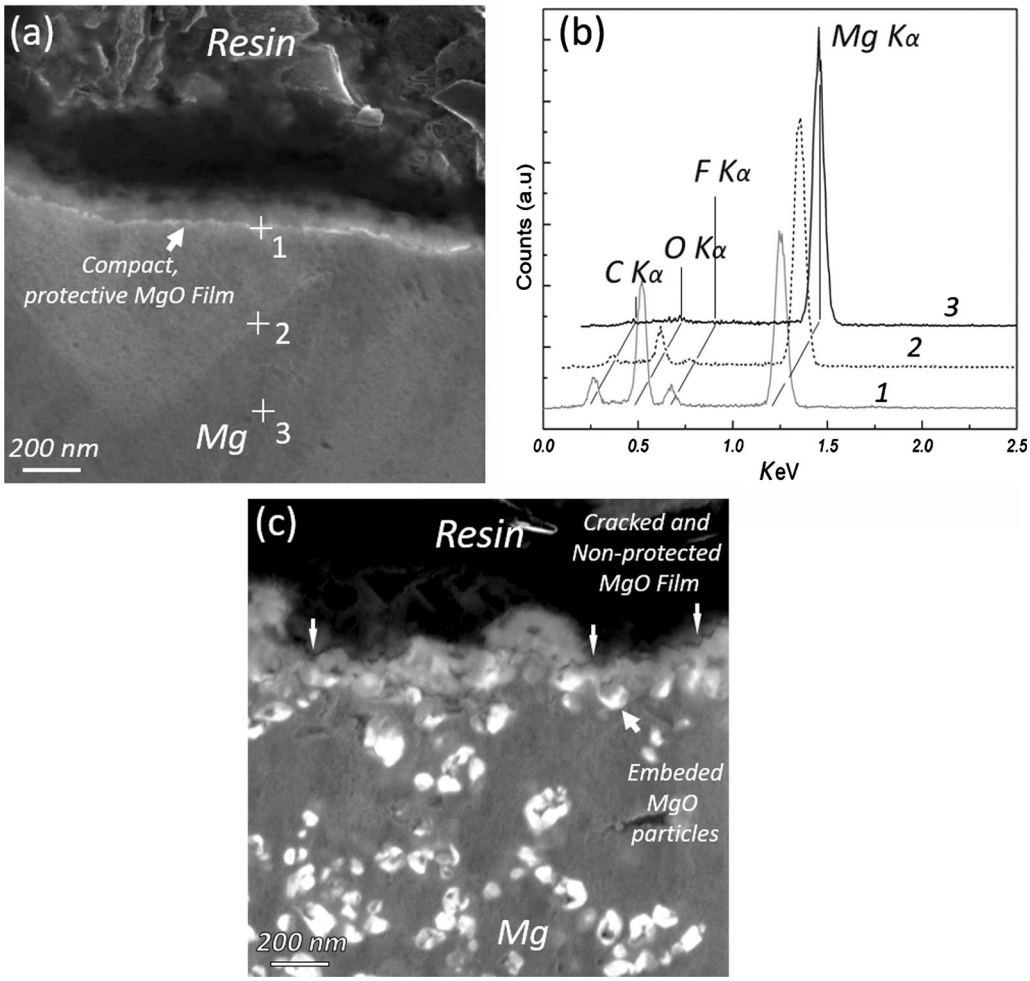

Fig. 10—The morphology of MgO films/particles formed on the surface of CP Mg ingot and the related EDS spectra. (*a*) SE SEM image showing a compact MgO film on the surface; (*b*) EDS spectra taken from point 1, 2, 3 marked in (a); and (*c*) SE SEM image showing a cracked MgO film with MgO particles occurring beneath the film. For clarity, the spectra in (b) were shifted to the top-right direction.

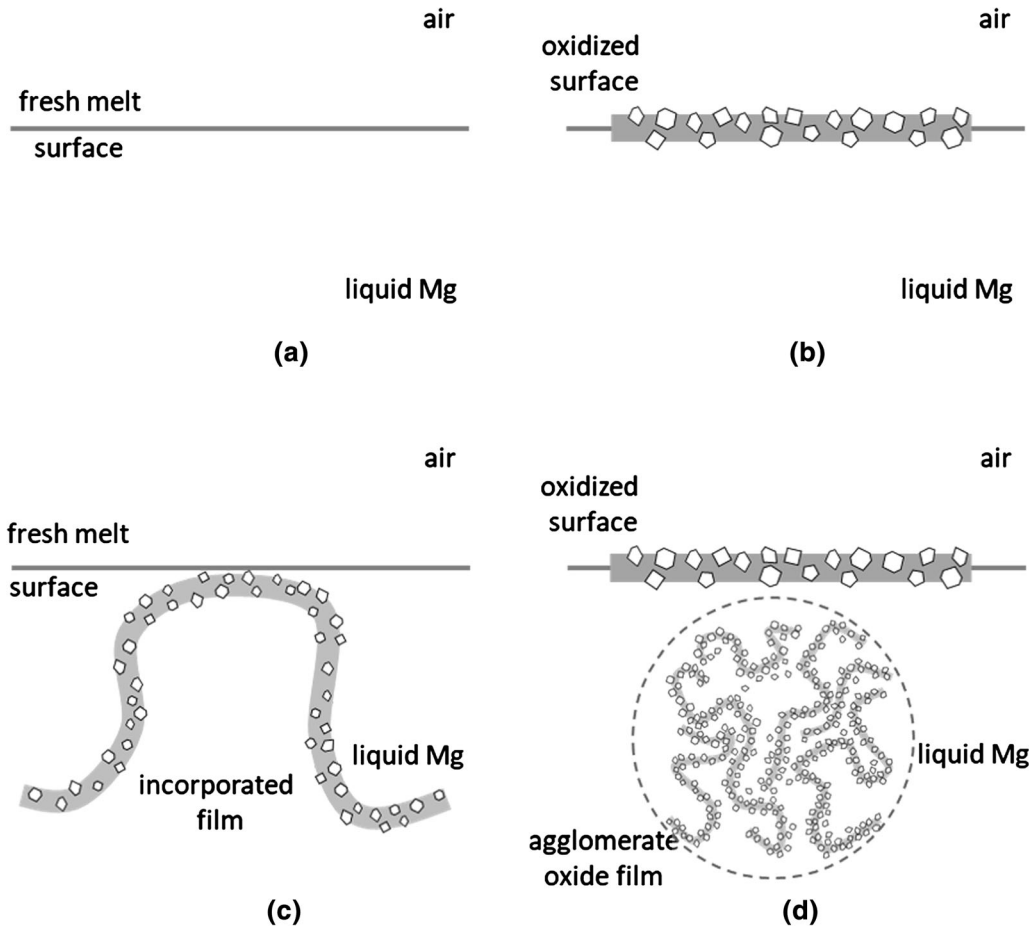

Fig. 11—Schematics showing the formation of the young film. (*a*) The fresh liquid Mg surface exposed to the air; (*b*) formation of a liquid oxide film consisting of discrete MgO particles; (*c*) incorporation of the oxide film into the melt; and (*d*) formation of a micron-scale agglomeration of the young oxide films.

of CP-Mg (Figure 10(c)), the sole appearance of the octahedral MgO particles suggests that the {111} terminations should be more stable than {100} terminations in terms of surface energy in such an oxidation environment. This seems contradictory with the fact that the surface energy of {111} facets in MgO is known to be higher than that of {100} facets[41] due to the polarity of MgO resulting from the crystal structure under a dry environment. However, the alteration of the surface energy of a crystal is achievable through various methods.[43–47] For instance, hydroxylation has been proposed as a means to stabilize the polar {111} facet of MgO into a non-polar state,[44,46] at which point lowering the surface energy becomes achievable. In this case, since {111} MgO was also found in CP Mg and given the absence of Al segregation on any facets in Mg-9Al, adsorption or segregation of alloying elements should be excluded as the reason for the depolarization of the {111} facet. It could be speculated that the Mg melt, which has a good wetting behavior on the octahedral MgO particles (Figures 1 to 4, 7 and 10(c)), might play a role in switching MgO into an octahedral morphology in a nonpolar manner. The surrounding liquid Mg is able to provide free electrons to eliminate the polar effect and stabilize the surface. This conjecture agrees with the theory proposed by Goniakowski,[47] who showed that metal screening is an effective way of polarity compensation for MgO nanoribbons.

Kinetics is more likely to affect the growth of {111} MgO at the melt surface, where both the relatively lower temperature (liquidus *vs* burning) and the obstacle of surface oxide film lead to the lower supply rate of oxygen. In terms of crystallography, the stacking sequence in a MgO crystal is '…ABCABC…' for {111} 'Mg' and {111} 'O' planes stacking alternatively on each other. In contrast, the {100} facet is uniformly composed of Mg cations and O anions in a 1:1 ratio. If the lack of oxygen is a limiting factor, the growth of {100} planes should be favored as 50 pct less oxygen is required compared to a full stacking unit of {111} 'O' plane. Therefore, the growth along the ⟨100⟩ direction becomes faster than along the ⟨111⟩ direction. This leads to the gradual disappearance of {100} facets and thus the predominance of {111} facets. In contrast, the higher diffusion rate and abundant oxygen source during the formation of {100} MgO make the growth rate dependent on the surface energy only, so that the shape of MgO is fully determined by equilibrium thermodynamics. In addition, the overall relatively low growth kinetics may account for the smaller size of {111}

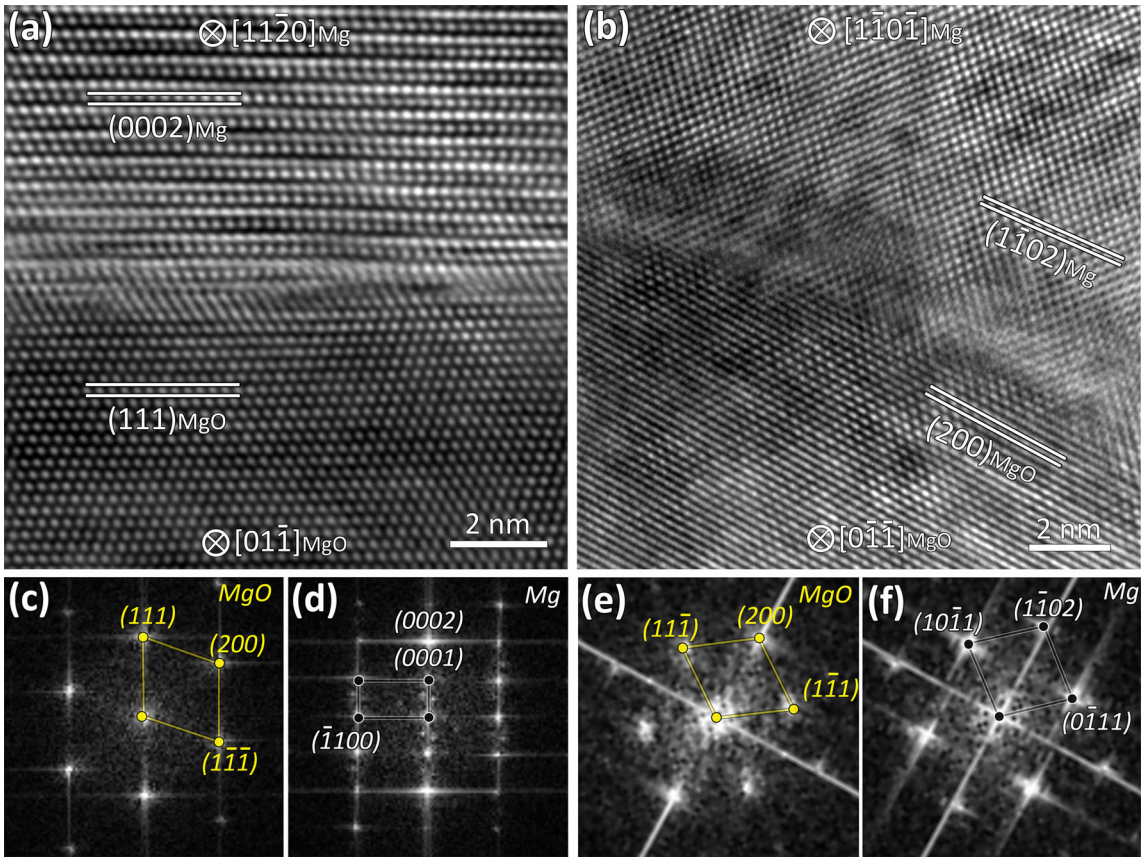

Fig. 12—(*a*, *b*) HRTEM images of MgO/Mg interfaces and (*c* through *f*) the corresponding fast Fourier transform (FFT) patterns showing two types of orientation relationships: OR1, $(111)[01\bar{1}]_{MgO}//(0002)[11\bar{2}0]_{Mg}$ in (a, c, d) and OR2, $(200)[0\bar{1}\bar{1}]_{MgO}//(1\bar{1}02)[1\bar{1}0\bar{1}]_{Mg}$ in (b, e, f).

MgO than {100} MgO, as shown in Figure 8. Moreover, the kinetics makes it possible that some {100} terminations are retained to form cuboctahedral MgO, as evidenced in Figures 4 and 5 where the smaller {111} MgO particles still have {100} facets that are hypothesized to shrink when the particle grows larger. A recent thermodynamics study of the Mg-O binary phase diagram confirmed the higher than expected solubility of O in liquid Mg,[48] providing evidence that the growth of a MgO particle inside the melt can proceed and ultimately the {100} facet will disappear.

D. *Effect of MgO on Grain Refinement*

No matter to which morphology the MgO particle belongs, the truncated facets are composed of either a combination of {111} and {100} facets for octahedral MgO or of the sole {100} facets for cubic MgO. Therefore, the terminating surface available for heterogeneous nucleation of α-Mg should be either {111} or {100} plane in terms of crystallography. As shown in the HRTEM images and corresponding Fourier transform (FFT) patterns in Figure 12, two well-defined ORs were detected:

OR1 for {111} facet, $(111)[01\bar{1}]_{MgO}//(0002)[11\bar{2}0]_{Mg}$;

OR2 for {100} facet, $(200)[0\bar{1}\bar{1}]_{MgO}//(1\bar{1}02)[1\bar{1}0\bar{1}]_{Mg}$.

They are consistent with the ORs reported previously.[25,27] According to these ORs, the lattice misfit (*f*) between the solid (S) and the nucleating substrate (N) and can be calculated using the equation below:[31]

$$f = \frac{d_s - d_N}{d_s} \times 100\,\text{pct} \qquad [1]$$

where d_S and d_N are the interatomic spacings along the matching directions for the solid and the nucleating substrate, respectively. The calculated lattice misfits are tabulated in Table III in comparison with that for the Zr/Mg system.

Nucleation potency is affected by lattice misfit,[31] substrate surface roughness[49] and chemical interaction between substrate and the liquid.[50] In the absence of information of the latter two factors, lattice misfit is usually used as an indicator of nucleation potency; the smaller the lattice misfit, more potent the substrate for heterogeneous nucleation. From Table III it is seen that the lattice misfit, *f* is 7.86 pct for both {111} MgO and {100} MgO substrates. This value is much larger than the misfit between Zr and α-Mg (0.5 pct). This suggests that MgO requires a larger undercooling than Zr to nucleate α-Mg and thus serves a relatively impotent

Table III. Crystallographic Data of Mg,[52] MgO[34] and Zr[53] and the Calculated Lattice Misfit Based on the Observed and Reported ORs at 650 °C

Interface, (N/S)	Lattice Parameter (Å) at 650 °C	ORs: $(h'k'l')[u'v'w']_N$ // $(hkl)[uvw]_S$	$d_{[u'v'w']}$ (Å)	$d_{[uvw]}$ (Å)	f (Pct)
MgO/Mg	N: FCC, a = 4.2476	$(111)[01\bar{1}]_{MgO}//(0002)[11\bar{2}0]_{Mg}$	$\langle 011\rangle$	$\langle 11\bar{2}0\rangle$	7.86
	S: HCP, a = 3.2599, c = 5.3001		3.0036	3.2599	
		$(200)[0\bar{1}\bar{1}]_{MgO}//(1\bar{1}02)[1\bar{1}0\bar{1}]_{Mg}$, as equivalent to $(200)[01\bar{1}]_{MgO}//(1\bar{1}02)[11\bar{2}0]_{Mg}$	$\langle 011\rangle$	$\langle 11\bar{2}0\rangle$	7.86
			3.0036	3.2599	
Zr/Mg	N: HCP, a = 3.2435, c = 5.1838	$(0002)[11\bar{2}0]_{Zr}//(0002)[11\bar{2}0]_{Mg}$[54]	$\langle 11\bar{2}0\rangle$	$\langle 11\bar{2}0\rangle$	0.50
	S: HCP, a = 3.2599, c = 5.3001		3.2435	3.2599	

Note that the lattice parameter (Å) for each phase at room temperature (20 °C) is: Mg, a = 3.2092, c = 5.2121; MgO, a = 4.2113; Zr, a = 3.233, c = 5.148. while the coefficient of thermal expansion (1/K) is: Mg: //a 25.1*10^{-6}, //c 26.8*10^{-6},[55] MgO: 13.68*10^{-6},[56] and Zr: //a 5.15*10^{-6}, //c 11.03*10^{-6}.[53]

substrate. In addition, recent DFT work by Fang and Fan[51] revealed that the chemical interaction between the O-terminated {111} MgO and liquid Mg gives rise to an ordered Mg layer on the MgO surface, and that this ordered Mg layer is atomically rough due to the existence of around 8 pct of vacancies. The atomically rough surface makes {111} MgO even more impotent for nucleation of Mg,[49] leading to a relatively high nucleation undercooling (ΔT_n).

Closely related to grain refinement is the grain initiation behavior, which is determined by the free growth undercooling ΔT_{fg} that is a function of substrate size.[30] For potent substrates $(\Delta T_n < \Delta T_{fg})$, such as Zr particles, grain initiation occurs on the largest particle first, and followed by progressively smaller ones. This behavior has been named as progressive grain initiation (PGI).[57] In contrast to the above situation, for more impotent substrates ($\Delta T_n > \Delta T_{fg}$, for the largest particle(s)), such as MgO particles, grain initiation occurs in an explosive manner, which is referred to as explosive grain initiation (EGI).[57] In Mg-alloy melts, MgO particles have a small size (d_0), a narrow size distribution (σ) and a large number density (~ 10^{17} cm^3) in the melt..[58] In this case ΔT_n is larger than the ΔT_{fg} required by quite a large amount of MgO particles, once nucleation undercooling is satisfied these MgO particles can initiate the Mg grains immediately after nucleation. This will lead to a significant proportion of grains being initiated in an "explosive" manner and results in a reduced grain size.[57,59] In practice, it has been confirmed that the well-dispersed native MgO particles can lead to significant grain refinement in Mg alloys.[25,27,54,57]

V. CONCLUSIONS

(1) The native MgO in CP Mg and Mg-9Al alloy exists as three distinctive morphology types at the micron scale: young film, old film and ingot skin. All of them consist of discrete and densely populated MgO particles with a nano-scaled size in the Mg melt.

(2) {111} MgO particles were observed in both CP-Mg and Mg-9Al alloy. The morphology of the particles consists mainly of {111} facets and some portions of {100} facets, depending on the growth kinetics. The size distribution follows a log-normal, with a mean size of 68 nm in CP-Mg and 84 nm in Mg-9Al.

(3) {100} MgO particles were also observed in both CP-Mg and Mg-9Al alloy, and their morphology consists of six {100} facets. The size distribution follows a log-normal function in both cases, with a mean size of 85 nm in CP-Mg and 93 nm in Mg-9Al.

(4) It is suggested that the {111} MgO particles originate from the oxidation of liquid Mg. The polar {111} facet can be stabilized by a Mg screening effect, and its continued existence through the particle growth is kinetically favored.

(5) It is suggested that {100} MgO is the product of oxidation of Mg in the vapor phase where the {100} faceted terminations are favorable in terms of thermodynamics and kinetics.
(6) Based on the experimentally observed orientation relationships for {111} and {100} MgO, the lattice misfits between MgO and α-Mg are calculated both as 7.86 pct. The relatively high misfit value suggests that MgO is impotent for heterogeneous nucleation of α-Mg. However, in the explosive grain initiation scheme, the native MgO particles can still offer significant grain refinement of Mg alloys.

ACKNOWLEDGMENTS

EPSRC is gratefully acknowledged for financial support under Grant Number EP/N007638 /1. The SuperSTEM Laboratory is the U.K National Research Facility for Advanced Electron Microscopy, supported by EPSRC. SHW gratefully acknowledges the China Scholarship Council (CSC) for financial support and ETC in Brunel University for providing access to the facilities. SHW wishes to thank Dr Feng Wang and Dr Feng Gao for their invaluable discussions on the content of this article, Mr Peter Lloyd for help on casting experiments and Dr Chamini Mendis for help on the deep etching experiment.

OPEN ACCESS

REFERENCES

1. W.J. Joost: *Magnesium Technology 2014*, Wiley, Hoboken, 2014, pp. 3–4.
2. H.S. Tathgar, P. Bakke, and T.A. Engh: *Magnesium Alloys and Their Applications*, WILEY-VCH Verlag GmbH, Weinheim, 2000, pp. 767–79.
3. S. Lunsin, A. Elsayed, and C. Ravindran: *Int. Mater. Rev.*, 2013, vol. 58, pp. 419–36.
4. W.D. Griffiths and N.W. Lai: *Metall. Trans. A*, 2007, vol. 38A, pp. 190–96.
5. A. Elsayed and C. Ravindran: *J. Mater. Eng. Perform.*, 2014, vol. 23, pp. 628–36.
6. N.B. Pilling and R.E. Bedworth: *J. Inst. Met.*, 1923, vol. 29, pp. 529–82.
7. T. Marker: Report No. DOT/FAA/AR-11/3, Federal Aviation Administration, Atlantic, January 2013.
8. A.A. Luo: *Int. Mater. Rev.*, 2004, vol. 49, pp. 13–30.
9. J. Campbell: *Complete Casting Handbook: Metal Casting Processes, Metallurgy, Techniques and Design*, 2nd ed., Butterworth-Heinemann, Oxford, 2015.
10. M.O. Pekguleryuz, K. Kainer, and A. Kaya: *Fundamentals of Magnesium Alloy Metallurgy*, Elsevier, Amsterdam, 2013.
11. A. Mirak, C.J. Davidson, and J.A. Taylor: *Corros. Sci.*, 2010, vol. 52, pp. 1992–2000.
12. G. Pettersen, E. Øvrelid, G. Tranell, J. Fenstad, and H. Gjestland: *Mater. Sci. Eng. A*, 2002, vol. 332, pp. 285–94.
13. T.W. Lee, H.W. Park, H. Lim, S.K. Kim, and S.H. Lim: *J. Alloys Compd.*, 2017, vol. 714, pp. 397–408.
14. B.S. You, W.W. Park, and I.S. Chung: *Scr. Mater.*, 2000, vol. 42, pp. 1089–94.
15. G. Song and A. Atrens: *Adv. Eng. Mater.*, 1999, vol. 1, pp. 11–33.
16. F. Czerwinski: *Int. Mater. Rev.*, 2015, vol. 60, pp. 264–96.
17. Q. Tan, A. Atrens, N. Mo, and M.X. Zhang: *Corros. Sci.*, 2016, vol. 112, pp. 734–59.
18. E.F. Emley: *Principles of Magnesium Technology*, Pergamon Press, Oxford, 1966.
19. S.L. Couling, F.C. Bennett, and T.E. Leontis: *Light Met. Age*, 1977, vol. 35, pp. 12–21.
20. A. Prasad, Z. Shi, and A. Atrens: *Adv. Eng. Mater.*, 2012, vol. 14, pp. 772–84.
21. J. Campbell: *Metall. Trans. B*, 2006, vol. 37B, pp. 857–63.
22. C.S. Goh, M. Gupta, J. Wei, and L.C. Lee: *J. Compos. Mater.*, 2007, vol. 41, pp. 2325–35.
23. H. Hall: *Magnes. Rev. Abs.*, 1945, vol. 3, pp. 68–72.
24. Y. Lee: Doctoral dissertation, The University of Queensland, 2002.
25. Z. Fan, Y. Wang, M. Xia, and S. Arumuganathar: *Acta Mater.*, 2009, vol. 57, pp. 4891–901.
26. B. Jiang: Doctoral dissertation, Brunel University, 2013.
27. Y. Wang, G. Peng, and Z. Fan: *Magnesium Technology*, Springer International Publishing, New York, 2017, pp. 99–106.
28. Z. Fan, B. Jiang, and Y.B. Zuo. 2011. Apparatus and method for liquid metals treatment. PCT/GB2011/051744 UK.
29. Y. Wang, Z. Fan, X. Zhou, and G.E. Thompson: *Philos. Mag. Lett.*, 2011, vol. 91, pp. 516–29.
30. A.L. Greer, A.M. Bunn, A. Tronche, P.V. Evans, and D.J. Bristow: *Acta Mater.*, 2000, vol. 48, pp. 2823–35.
31. Z. Fan: *Metall. Trans. A*, 2013, vol. 44A, pp. 1409–18.
32. J. Schindelin, I. Arganda-Carreras, E. Frise, V. Kaynig, M. Longair, T. Pietzsch, S. Preibisch, C. Rueden, S. Saalfeld, B. Schmid, J.-Y. Tinevez, D.J. White, V. Hartenstein, K. Eliceiri, P. Tomancak, and A. Cardona: *Nat. Methods*, 2012, vol. 9, pp. 676–82.
33. S.J. Randolph, J.D. Fowlkes, and P.D. Rack: *Crit. Rev. Solid State Mater. Sci.*, 2006, vol. 31, pp. 55–89.
34. M. Boiocchi, F. Caucia, M. Merli, D. Prella, and L. Ungaretti: *Eur. J. Mineral.*, 2001, vol. 13, pp. 871–81.
35. G. Wulff: *Zeitschrift für Kristallographie*, 1901, vol. 34, pp. 449–530.
36. F. Czerwinski: *Acta Mater.*, 2002, vol. 50, pp. 2639–54.
37. T. Leontis and F. Rhines: *Trans. Am. Inst. Min.*, 1946, vol. 166, pp. 265–94.
38. M.J. Balart and Z. Fan: *Int. J. Cast Met. Res.*, 2014, vol. 27, pp. 167–75.
39. R.D. Heidenreich: *Phys. Rev.*, 1942, vol. 62, pp. 291–92.
40. M. Peter: *J. Phys. Chem. Solids*, 1968, vol. 29, pp. 689–97.
41. F. Finocchi and J. Goniakowski: *Surf. Sci.*, 2007, vol. 601, pp. 4144–48.
42. J. Benard: *Adsorption on Metal Surfaces: An Integrated Approach*, Elsevier, Amsterdam, 1983, pp. 44–99.
43. J. Zhang, Q. Kuang, Y. Jiang, and Z. Xie: *Nano Today*, 2016, vol. 11, pp. 661–77.
44. K. Refson, R.A. Wogelius, D.G. Fraser, M.C. Payne, M.H. Lee, and V. Milman: *Phys. Rev. B*, 1995, vol. 52, pp. 10823–826.
45. R. Hacquart and J. Jupille: *Chem. Phys. Lett.*, 2007, vol. 439, pp. 91–94.

46. P. Geysermans, F. Finocchi, J. Goniakowski, R. Hacquart, and J. Jupille: *Phys. Chem. Chem. Phys.*, 2009, vol. 11, pp. 2228–33.
47. J. Goniakowski, L. Giordano, and C. Noguera: *Phys. Rev. B.*, 2013, vol. 87, pp. 1–10.
48. S.M. Liang and R. Schmid-Fetzer: *J. Eur. Ceram. Soc.*, 2018, vol. 38, pp. 4768–85.
49. B. Jiang, H. Men, and Z. Fan: *Comput. Mater. Sci.*, 2018, vol. 153, pp. 73–81.
50. C.M. Fang, H. Men, and Z. Fan: *Metall. Mater. Trans. A*, 2018, vol. 49A, pp. 6231–42.
51. C.M. Fang and Z. Fan: *Metall. Trans. A*, 2020, vol. 51A (2), pp. 788–97.
52. B. Predel and K. Hülse: *Chemischer Informationsdienst*, 1979, vol. 10, pp. 690–96.
53. J. Goldak, L.T. Lloyd, and C.S. Barrett: *Phys. Rev.*, 1966, vol. 144, pp. 478–84.
54. G.S. Peng, Y. Wang, and Z. Fan: *Metall. Trans. A*, 2018, vol. 49A, pp. 2182–92.
55. R.S. Krishnan, R. Srinivasan, and S. Devanarayanan: *Thermal Expansion of Crystals*, 1st ed., Pergamon Press, Oxford, 1979, pp. 124–25.
56. M.A. Durand: *Physics*, 1936, vol. 7, pp. 297–98.
57. Z. Fan: *Magnesium 2018 – The 11th Int. Conf. Magnesium Alloys Their Appl.*, Brunel University Press, Beaumont Estate, Old Windsor, UK, 2018, pp. 7–16.
58. H. Men, B. Jiang, and Z. Fan: *Acta Mater.*, 2010, vol. 58, pp. 6526–34.
59. B. Jiang and Z. Fan: *Proceedings of the 6th Decennial International Conference on Solidification Processing (SP17)*, Brunel University Press, Beaumont Estate, Old Windsor, UK, 2017, pp. 25–28.